Nanoscale

Accepted Manuscript

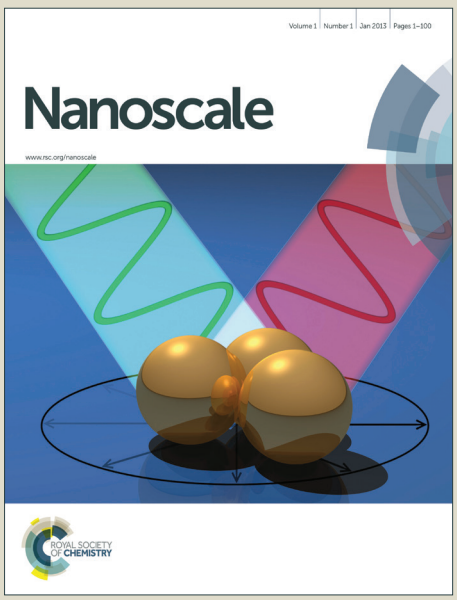

ROYAL SOCIETY OF CHEMISTRY

www.rsc.org/nanoscale

Journal Name

RSCPublishing

ARTICLE

Improved electronic coupling in hybrid organic-inorganic nanocomposites employing thiol-functionalized P3HT and non-toxic bismuth sulfide nanocrystals

Cite this: DOI: 10.1039/xoxxoooooox

Received ooth January 2012,
Accepted ooth January 2012

DOI: 10.1039/xoxxoooooox

www.rsc.org/

L. Martínez[a], S. Higuchi[b], A. J. MacLachlan[c], A. Stavrinadis[a], N. C. Miller[a], S. L. Diedenhofen[a], M. Bernechea[a], S. Sweetnam[d], J. Nelson[c], S. A Haque[c], K. Tajima[e,f], G. Konstantatos[a*]

In this paper we employ a thiol-functionalized polymer (P3HT-SH) as a leverage to tailor the nanomorphology and electronic coupling in polymer-nanocrystal composites for hybrid solar cells. The presence of the thiol functional group allows for a highly crystalline semiconducting polymer film at low thiol contents and allows for improved nanomorphologies in hybrid organic-inorganic systems when employing non-toxic bismuth sulfide nanocrystals. Exciton dissociation efficiency and carrier dynamics at this hybrid heterojunction are investigated through photoluminescence quenching and transient absorption spectroscopy measurements, revealing a larger degree of polaron formation when P3HT-SH is employed, suggesting an increased electronic interaction between the metal chalcogenide nanocrystals and the thiol-functionalized P3HT. The fabricated photovoltaic devices show 15% higher power conversion efficiencies as a result of the improved nanomorphology and better charge transfer mechanism together with the higher opencircuit voltages arisen from the deeper energy levels of P3HT-SH.

A Introduction

Hybrid organic-inorganic systems can combine the advantages of low-cost and solution-processability of organic semiconductors with the infrared sensitivity and chemical stability of inorganic materials,[1] thus becoming a new platform for solution-processed optoelectronic devices such as photodetectors and solar cells.[2,3] Hybrid organic-inorganic photovoltaic devices take advantage of the recent developments in both the organic photovoltaic (OPV) and the inorganic nanocrystal (NC) and quantum dot communities. Novel low bandgap polymers, more suitable for single-junction solar harnessing architectures, such as poly[2,6-(4,4-bis-(2-ethylhexyl)-4H-cyclopenta[2,1-b;3,4-b']dithiophene)-alt-4,7-(2,1,3-benzothiadiazole)] (PCPDTBT) have been recently combined with cadmium selenide (CdSe).[4] Also, solar cells based on poly[2,6-(N-(1-octylonyl)dithieno[3,2-b:20,30-d]pyrrole)-alt-4,7-(2,1,3-benzothiadiazole)] (PDTPBT) and lead sulfide (PbS) quantum dots have been recently demonstrated.[5] The reported power conversion efficiencies (PCEs) using the two aforementioned material combinations are nowadays approaching those attained in analogous systems employing the well-established fullerene derivatives, such as phenyl-C61-butyric acid methyl ester (PCBM).

Despite the recent progress achieved in photovoltaic performance, hybrid organic-inorganic nanocomposites still have to tackle many challenges. In addition to the further improvement of PCEs, the field also requires the exploration of new nanomaterials based on non-toxic elements, to ease off environmental and regulatory concerns. Reports on inorganic nanocrystals that do not contain toxic heavy elements such as lead or cadmium are more limited and have achieved more modest power conversion efficiencies.[6–12] A major milestone towards higher PCEs relies in achieving higher charge separation and collection efficiencies in hybrid systems. A possible route to improve the charge dissociation efficiency is to improve the electronic coupling between the organic and the inorganic phases. This requires further exploration of the carrier dynamics in hybrid organic-inorganic nanocomposites in order to relate the hole and electron transfer rates with the recombination rate in these systems. Additionally, the probability of exciton dissociation could be maximized through control over nanomorphology with domain sizes smaller than or comparable to the exciton diffusion length. The vast majority of the research on hybrid organic-inorganic solar cells has relied so far on the random formation of nanodomains following a similar approach as the bulk heterojunction (BHJ) employed in all-organic solar cells.[13] Recently, block copolymers have been employed as additives to improve the compatibility of conjugated semiconducting polymers and inorganic

nanocrystals.[14] Also, block copolymers have been modified to incorporate amine and ether functional groups.[15,16] When mixed with inorganic nanocrystals, the presence of the functional group is believed to increase the affinity of these polymers to the polar nanocrystal surface.[17] Accordingly, these polymers have provided for a better control over the nanomorphology of the active layer, leading to a more uniform NC dispersion inside the polymer matrix. PCE in these new systems has however, not benefitted from the improvements on nanomorphology, resulting in similar or worse photovoltaic performance. We hypothesize that this might be due to a large distortion of the polymer's crystallinity in the presence of the inorganic nanocrystals or due to a weak electrical interaction between the polymer and the NCs. Our first goal is to investigate the structural properties of the functionalized block copolymer as well as assess the electronic interaction between inorganic NCs and semiconducting polymers, addressing the role of functional groups in the charge separation efficiency and then demonstrate the potential of the approach in hybrid solar cells.

In doing so, we develop the synthesis of a thiol-functionalized block copolymer based on poly(3-alkylthiophene) (P3HT) and study its structural properties and the electronic interaction with non-toxic bismuth sulfide (Bi_2S_3) nanocrystals through grazing angle x-ray diffraction, photoluminescence and transient induced absorption spectroscopy methods. We also investigate the use of this nanocomposite as a hybrid organic-inorganic photovoltaic system. We find that both polymers exhibit similar degrees of long-range crystallinity, although the subtle differences observed, point towards a minor perturbation of the P3HT packing due to the presence of the thiol-functional group. The solar cells show 15% higher PCEs when employing this new thiol-functionalized block copolymer compared to those attained using non-functionalized P3HT. This occurs as a result of an increased electronic interaction and improved nanomorphology, which result in an increased exciton dissociation efficiency obtained when employing the thiol-functionalized block copolymer.

B Synthesis and characterization of the thiol-functionalized block copolymer

A new block copolymer functionalized with a thiol (SH) group, based on hexylthiophenes (namely P3HT-SH) was synthesized as sketched in Figure 1. Polymer synthesis relies on the controlled synthesis of regioregular poly(3-alkylthiophene)s by Grignard metathesis (GRIM) method and quasi-living polymerization with Ni(dppp)Cl2 based on the reports by McCullough and Yokozawa.[17,18] In the first step, the GRIM product of 2-bromo-5-iodo-3-hexylthiophene was polymerized with the Ni catalyst to obtain the P3HT living polymer. The GRIM product of 2-bromo-3-hexyl-5-iodo(6-bromohexyl)thiophene was subsequently added to the living polymer solution to extend the polymer chain by the chain-growth mechanism to form the block copolymer.

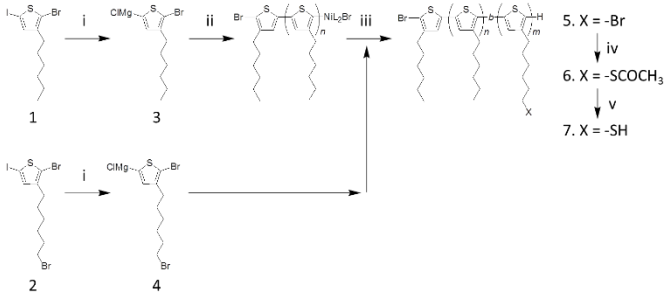

Figure 1 Synthetic Route for Thiol-functionalized Diblock Copolymers. Reagents and conditions (i) THF, i-PrMgCl, 0 °C; (ii)Ni(dppp)Cl2, 40 °C; (iii) 4, 40 °C; (iv) THF, Potassium thioacetate, Reflux; (v) THF, Lithium aluminum hydride, 30 °C.

The chain length in the diblock copolymer (m and n) was controlled by changing the monomer feed ratios. The final chemical structure of the synthesized block copolymer is depicted in Figure 2a. Thiol groups were attached at the end of the side chains on 3-position of thiophene rings of the second block. The block ratio in the copolymer, defined as m/(m+n), synthesized in this study was changed from 6% to lower than 1% (Figure S2 to S7). Unless otherwise stated, the polymer with the content of the thiol unit lower than 1% was used for this study, since the polymers with higher thiol contents significantly lower the device performance. Although the length of the second block was small, the polymers were synthesized by well-established GRIM and Ni-catalyzed quasi-living polymerization which also allow for larger block copolymer ratios. The motivation for choosing a thiol functional group is twofold. On one hand, its strong binding ability to metals could lead to a superior electronic interaction between the polymer and the NCs' surface.[1] On the other hand, available dangling bonds present at the metal chalcogenide nanocrystals surface can be efficiently passivated by the thiol group, thus reducing undesired trap assisted carrier recombination.[19]

Optical absorption in thin film of the thiol-functionalized block copolymer (P3HT-SH Figure 2b) shows a slight blue-shift of the absorption peak and slightly less pronounced shoulder at around 600 nm which indicates that P3HT-SH retains most of the crystallinity of P3HT despite the presence of the thiol group. We performed grazing incidence x-ray diffraction (GI-XRD) to further assess the polymer order. Figure 2c shows the two-dimensional GI-XRD images and Figure 2d shows the out-of-plane x-ray diffraction patterns of both P3HT and P3HT-SH demonstrating a prominent (100) peak at Qz=0.38Å-1. We observe that the relative intensities between the (100) peak and the secondary and tertiary diffraction peaks are comparable for P3HT and P3HT-SH, again indicating similar extents of crystallinity in the two polymers. Figure 2e shows the radial integration of the π-stacking peak at Q~1.7 Å-1. As evidenced in this figure, the center of this peak for P3HT-SH is slightly shifted to smaller Q compared to P3HT. Fitting the curves with Laurentzian functions also revealed a wider peak for P3HT-SH (0.167 Å-1) compared to P3HT (0.149 Å-1). The shift and increased width indicate that the polymer packing might be slightly disturbed by the presence of the thiol group in the thiol-functionalized block copolymer. Nevertheless, the structural results indicate that both polymers have a similar crystallinity degree and optical bandgap, making P3HT-SH an interesting semiconducting polymer for solar applications in combination with metal chalcogenide nanocrystals.

ARTICLE

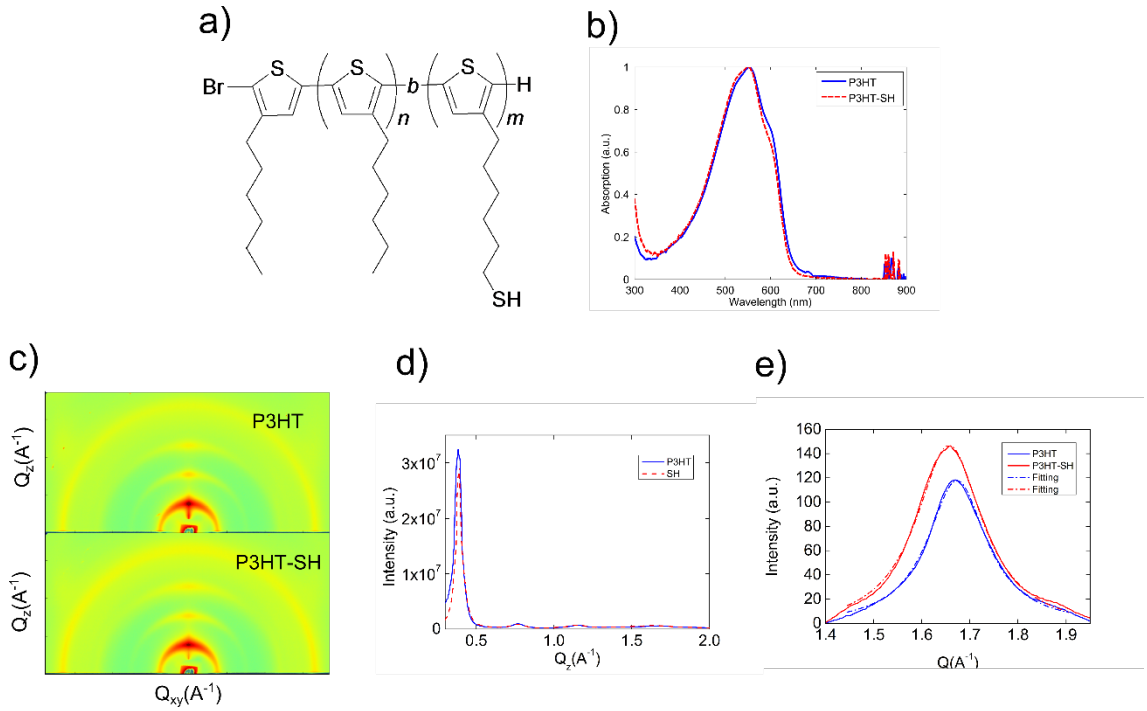

Figure 2 (a) Chemical structure of thiol-functionalized block copolymer P3HT-SH and (b) normalized optical absorption of P3HT (blue solid line) and P3HT-SH (red dashed line) in spincoated films on glass substrates.(c) 2D GI-XRD pattern of P3HT (top) and P3HT-SH (bottom) (d) GI-XRD diffraction pattern along the out-of-plane direction of P3HT (blue solid line) and P3HT-SH (red dashed line) (e) Radial integration of the pi-stacking peak at Q~1.7 $Å^{-1}$ from the 2D GI-XRD pattern shown in c.

C Charge transfer studies

C1 Photoluminescence quenching

Photoluminescence quenching is a common technique used to measure the electronic interaction, i.e. charge transfer, between two molecules or between polymer and semiconductor nanocrystals.[20] Even highly efficient photovoltaic systems such as P3HT:PCBM do not show any significant photoluminescence (PL) quenching in solution,[21] indicating no specific intermolecular interaction between the two molecules. In those systems, photoluminescence is dramatically quenched after film formation.[22] To investigate the affinity of the thiol-functionalized P3HT (P3HT-SH) polymer on the nanocrystal surface and the corresponding degree of electronic interaction between P3HT-SH and Bi_2S_3, we performed photoluminescence quenching studies in solution. We compared the intensity of the PL spectra of P3HT and P3HT-SH both before and after blending with Bi_2S_3 nanocrystals. Figure 3a shows the PL spectrum of P3HT-SH from which a strong quenching (~50%) after blending with Bi_2S_3 can be observed. This PL quenching is much larger than that observed for the Bi_2S_3:P3HT solution (~20%) as shown in Figure 3b. This suggests an efficient charge transfer between the P3HT-SH and the Bi_2S_3 NCs compared to P3HT and Bi_2S_3, as a result of anchoring of the P3HT-SH on the surface of Bi_2S_3 NCs, via the thiol moiety. It is noteworthy that no ligand exchange method has been employed to remove the original insulating oleic acid molecules from the surface of the bismuth sulfide nanocrystals. The slight (~20%) PL quenching observed in the Bi_2S_3:P3HT system can be attributed to an incomplete capping of the NCs' surface by the sterically large oleic acid molecule,[23] since in the latter system there is no thiol or functional group to replace the oleic acid molecule. Unpassivated bismuth atoms on the nanocrystal surface, might then weakly interact with the sulfur atom in the thiophene ring. Figure 3c shows the PL spectra of pristine P3HT and P3HT-SH in thin-film, both before and after blending with Bi_2S_3 nanocrystals. Bi_2S_3 has been reported as an efficient (~90%) quencher of P3HT's photoluminescence. [11] We also observe an almost complete PL quenching in solid state for both P3HT-SH and P3HT after blending with Bi_2S_3 NCs, which prevents us from comparison between P3HT and P3HT-SH in solid state. Therefore, an alternative method is required to quantitatively analyze and compare the charge separation process in these two hybrid organic-inorganic nanocomposites.

C2 Carrier dynamics

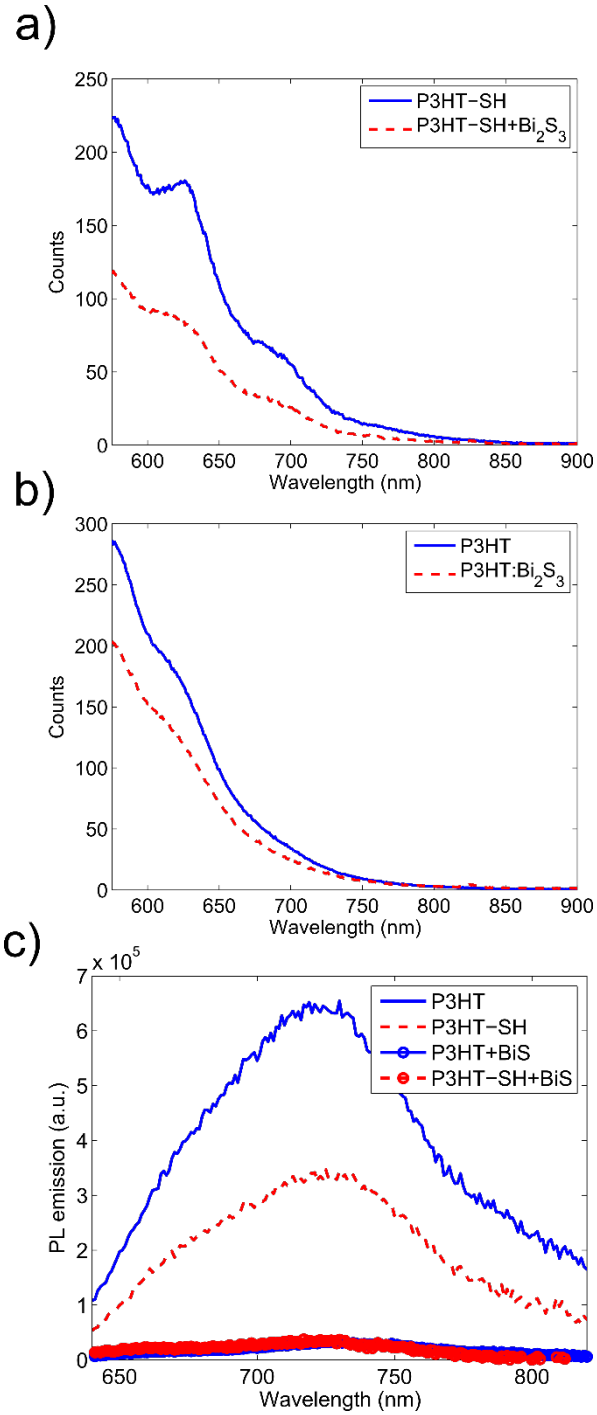

Figure 3 Photoluminescence (PL) spectra of (a) chloroform solutions of P3HT-SH (solid blue line) and blend of P3HT-SH:Bi2S3 (red dashed line) (b) chloroform solutions of P3HT (solid blue line) and blend of P3HT:Bi2S3 (red dashed line) and (c) PL spectra of P3HT (blue solid lines) and P3HT-SH (red dashed lines) in pristine films (solid lines) and in the blend films with Bi2S3(lines with circles). The PL spectrum for each sample has been normalized to the sample absorption at the excitation wavelength.

Transient absorption spectroscopy (TAS) can be employed to monitor the exchange of excited carriers between two different materials. Blend films of polymer with Bi_2S_3 nanocrystals were excited either with a visible laser pulse of 510 nm, therefore exciting both the polymer and the nanocrystals, or with a near-IR pulse of 700 nm, exciting only the nanocrystals. After visible excitation a broad peak centered around 1000 nm is observed for both P3HT and P3HT-SH (Figure S8) which we attribute to the P3HT hole polaron.[10] As this peak is similar for both polymer systems we are able to study the decay of the peak at 1000 nm for all samples. First considering the near-IR excitation (Figure 4a), where only the nanocrystals are absorbing the excitation light, the magnitude and lifetime of the signals in the P3HT and P3HT-SH samples are approximately the same. This suggests that the addition of the thiol group onto the P3HT alkyl chain has little effect on the hole transfer from the Bi_2S_3 nanocrystals to the polymer or on the recombination dynamics. When considering the visible excitation (Figure 4b), now exciting both the polymer and nanocrystals, the signal of the P3HT-SH samples is higher in comparison to the pristine P3HT. This suggests that the effect of addition of the thiol group is to increase the yield of electron injection from polymer to nanocrystal, while the hole transfer rate remains unchanged. This is attributed to morphological changes of the composite in which the P3HT-SH allows a more uniform blending with Bi_2S_3 NCs resulting in a larger polymer:NC interface lying within the exciton diffusion length of the polymer. After both visible and near-IR excitation we observe that a blend of both P3HT and P3HT-SH yields the highest amount of charges. We believe this is most likely due to an energy cascade that is set up in this system that drives charges away from the interface, a hypothesis that is discussed later in this article.

C3 Nanomorphology

We now consider the nanomorphology of the polymer:Bi_2S_3 films to further elucidate the role of the polymer components. As evidenced from cross-sectional scanning electron micrographs (SEM) presented in Figure 5, our devices based on P3HT-SH benefit from improved exciton dissociation efficiency due to a less aggregated nanomorphology. In Figure 5a we present the cross-sectional SEM of a hybrid device based on Bi_2S_3 and P3HT, where nanocrystal aggregation is evident, in contrast to Figure 5b, where we show the nanomorphology of a hybrid device based on Bi_2S_3 and the functionalized P3HT-SH polymer. It is noteworthy that tiny amounts of thiol functional group (<1%) are sufficient to provide for a less aggregated nanomorphology. Figure 5c shows the nanomorphology of the devices based on Bi_2S_3 nanocrystals and a 70:30 wt. mixture between P3HT and P3HT-SH. The reason for this weight ratio will be elucidated later on in this manuscript. We observe that the devices based on a mixture of P3HT and P3HT-SH preserve the finer morphology obtained when only P3HT-SH was employed. On the other hand, the devices based on Bi_2S_3 and P3HT reveal large (~100 nm) polymer-rich regions, where excitons are unlikely to find a neighboring dissociating interface, thus increasing the probability of exciton recombination. Exciton dissociation can only take place at the interface between NCs and P3HT, given the low dielectric constant of most semiconducting polymers. Upon splitting of the exciton, electrons are injected into the NCs while holes remain in the polymer phase. On the other hand, the devices based on the thiol-functionalized block copolymer benefit from an improved nanomorphology as evidenced by the more distributed NC dispersion observed in the cross-sectional SEM image. The smaller nanodomains observed employing thiol-functionalized block copolymer ensure that excitons are formed much closer to a dissociation interface throughout the whole active layer, increasing the

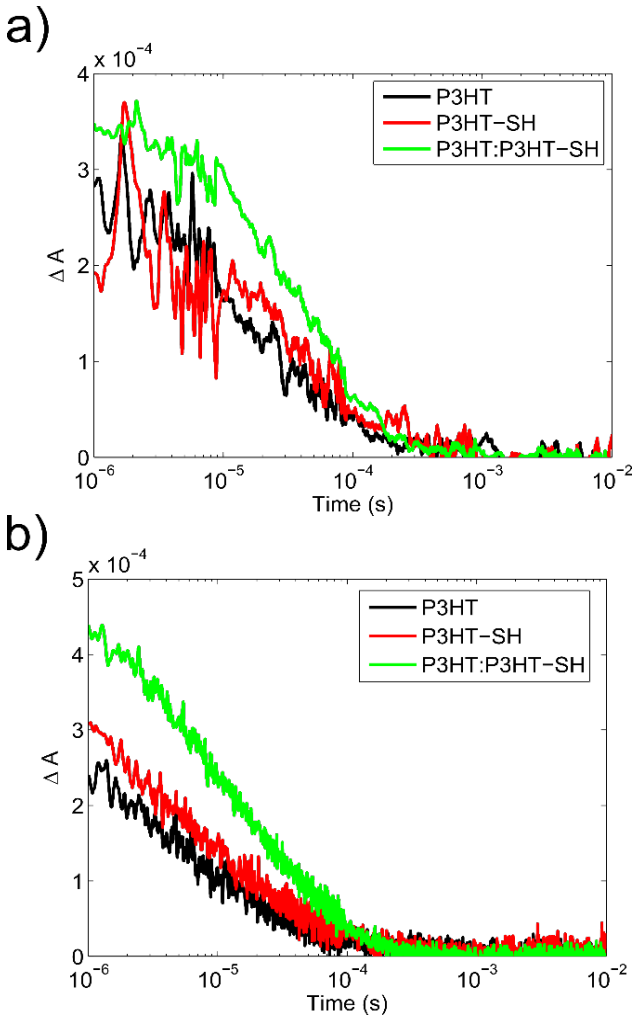

Figure 4 Transient absorption spectroscopy (TAS) measurements after (a) IR excitation (700 nm) and (b) visible excitation (510 nm) of EDT-exchanged blend films of: Bi_2S_3 and P3HT (black line), Bi_2S_3 and P3HT-SH (red line) and Bi_2S_3 and P3HT and P3HT-SH (green line).

exciton dissociation probability and ultimately increasing the yield of polaron formation.

C4 Energy levels

To further investigate the origin of the increased degree of polaron formation we address the possible formation of an energy gradient in systems based on ternary blends of Bi_2S_3, P3HT-SH and P3HT. For this purpose, we performed cyclic-voltammetry measurements (Figure 6a). From the onset of the first oxidation peak at ~5.5 eV, we found that the highest occupied molecular orbital (HOMO) level of P3HT-SH is approximately 50 meV deeper than that of regioregular P3HT. A similar offset was observed in photoelectron spectroscopy in air (Figure S9). We believe the presence of the thiol functional group in the polymer chain might cause perturbations in the packing of the polymer film, thus leading to the formation of a less crystalline phase, as already pointed out by the slight blue shift in optical absorption. The observed energetic change is much smaller than the 300 meV HOMO difference reported between crystalline and amorphous P3HT films,[24] which indicates that there is still a large degree of long-range ordering in the thiol-functionalized P3HT. Given the low amount of thiol

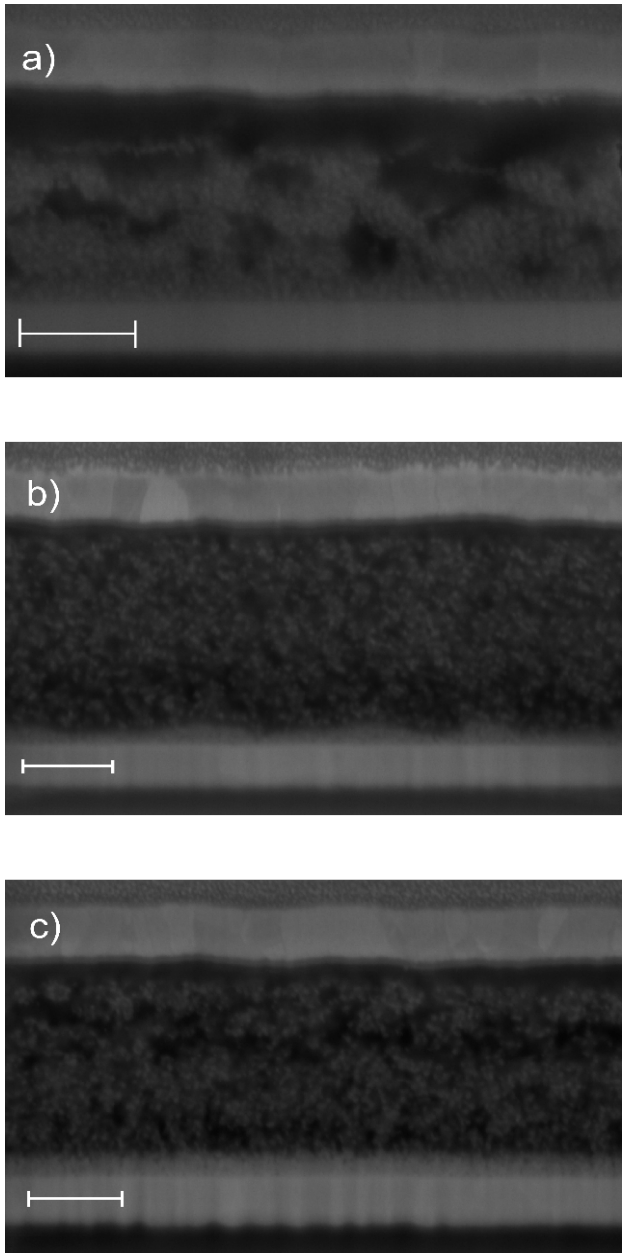

Figure 5 Cross-sectional scanning electron micrograph of (a) blends of Bi2S3:P3HT (b) Bi2S3:P3HT-SH and (c) Bi2S3 and a 70:30 wt. mixture of P3HT and P3HT-SH. Scale bars: 200 nm.

moieties employed in this study, we expect a minor influence of this small amorphous phase on the polymers' long-range electrical properties, which might become more severe with increasing block copolymer ratios.

Further evidence of a highly crystalline polymer phase is observed in field effect transistors measurements (FET, Figure S10), which yield P3HT-SH hole mobilities comparable to those obtained for highly regioregular P3HT.[25] The absolute position of the P3HT HOMO level (5.28 eV) with respect to vacuum was found to be close to that already reported using cyclic-voltammetry measurements.[26] The band diagram of the system based on a ternary blend of Bi_2S_3, P3HT-SH and P3HT is depicted in Figure 6b, showing the possible energy

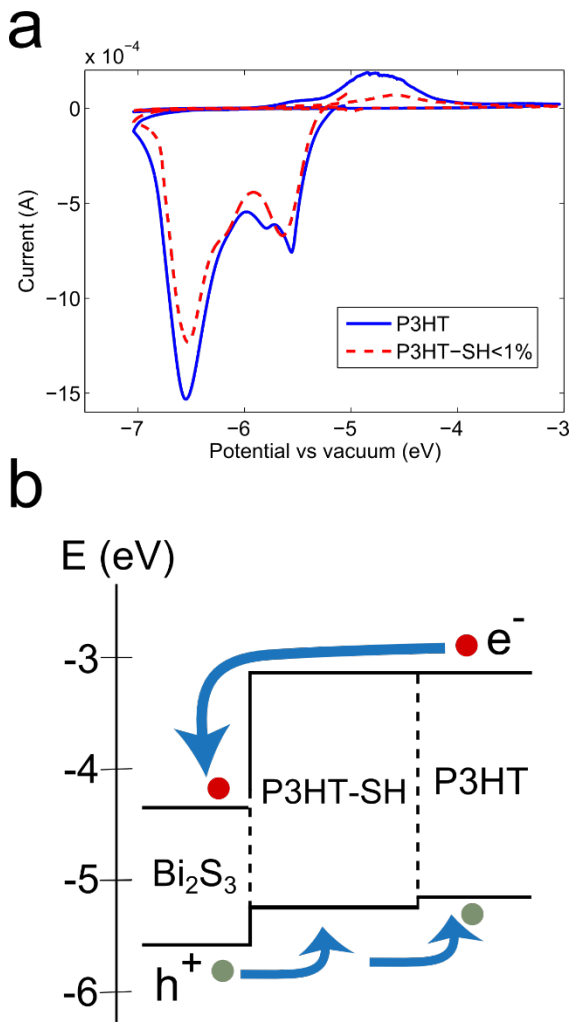

Figure 6 (a) Cyclic-voltammetry measurements of P3HT (blue solid line) and P3HT-SH<1% (red dashed line) and (b) the energy diagram of the hybrid organic-inorganic nanocomposites.

gradient driving photogenerated holes into the more crystalline P3HT. This energetic difference would as well act as a barrier opposing back recombination.[27] Both all-organic and all-inorganic solar cells that benefit from an energy cascade to improve charge separation have already been demonstrated. Its demonstration in hybrid polymer-nanocrystal systems has though yet to be reported.[28,29]

D Hybrid organic-inorganic solar cells

Encouraged by the stronger electronic interaction between P3HT-SH and Bi_2S_3 NCs observed in PL quenching and TAS measurements and from the improved nanomorphology, we fabricated photovoltaic devices. The device structure was ITO/ZnO/BHJ/P3HT/MoO3/Ag, where BHJ is a mixture of Bi_2S_3 nanocrystals and the polymers. Table 1 summarizes the performance of the solar cells. The fabricated photovoltaic devices using Bi_2S_3 and P3HT-SH showed a poor photovoltaic performance (PCE = 0.22%), as a result of a very low shortcircuit current density (Jsc). We attribute this to an excessive covering of the NC surface by the thiol-functionalized block copolymer, which ultimately hinders carrier hopping between adjacent nanocrystals. The same effect could also be the reason why previous works employing functionalized polymers in conjunction with inorganic nanocrystals have not achieved higher power conversion efficiencies, thus not benefiting from the demonstrated improved nanomorphology.[16] Therefore we decided to employ a mixture of P3HT and P3HT-SH as the electron donating material. Table S1 summarizes the figures of merit of the devices with different P3HT:P3HT-SH ratios. We observe that at an optimal P3HT to P3HT-SH weight ratio of 70:30 the highest power conversion efficiency (1.1%) is achieved due to a higher J_{sc} (7.6 $mAcm^{-2}$), indicative of a continuous percolation path for both carriers to the collecting electrodes. Charge separation mechanism in these devices drives the photogenerated holes into the polymer while electrons are injected into the bismuth sulfide nanocrystal phase and can reach the collecting electrode through hopping mechanism.[30]

Table 1 Photovoltaic performance of the hybrid solar cells based on bismuth sulfide and P3HT, thiol functionalized block copolymer and an optimized 70:30 vol. mixture of P3HT:P3HT-SH

Polymer	V_{oc} (V)	J_{sc} ($mAcm^{-2}$)	FF (%)	PCE (%)
P3HT	0.31±0.01	7.71±0.25	35.6±0.8	0.85±0.02
P3HT-SH	0.29±0.01	1.64±0.14	47.5±5.2	0.22±0.02
Optimized P3HT:P3HT-SH	0.34±0.01	7.19±0.30	41.0±1.3	1.01±0.04

We also found that the photovoltaic performance increases with a decrease in the content of the thiol moiety. The figures of merit of the solar cells based on 4%, 1% and <1% block copolymer ratios are presented in Table S2 and the ^{1}H NMR characterization of these polymers is presented in Figure S2 to S7. The higher photovoltaic performance with decreasing thiol content in the polymer network is also consistent with the aforementioned excessive covering of the NCs' surface by the P3HT-SH at high block copolymer ratios, isolating the nanocrystals and ultimately hindering the carrier hopping mechanism. Our best device showed V_{oc} of 0.34 V, J_{sc} of 7.6 $mAcm^{-2}$ and FF of 42% with a PCE of 1.1%, about 15% higher than that obtained with only P3HT. The current voltage characteristics of the solar cells based on pristine P3HT, pristine P3HT-SH and the optimized P3HT:P3HT-SH ratio are shown in Figure 7a, statistics are given in Table 1.The improved nanomorphology obtained employing P3HT-SH results in an increased exciton dissociation efficiency. The higher exciton dissociation efficiency together with the formation of an energy gradient that opposes back recombination lead to an increased FF compared to P3HT. External quantum efficiency (EQE) measurements are presented in Figure 7b. Beyond 650 nm Bi_2S_3:P3HT outperform as a result of better NC-NC interaction. Below 650 nm, the devices based on blends of Bi_2S_3:P3HT:P3HT-SH show higher EQE levels due to improved morphology and increased polaron formation yield as revealed in TAS measurements. Integration of the EQE multiplied by the solar radiation predicts a shortcircuit current density of 8.2 $mAcm^{-2}$, that is ~10% larger than the J_{sc} value of 7.6 $mAcm^{-2}$, obtained under simulated AM1.5G conditions. The reduction of the measured J_{sc} in comparison to the expected J_{sc} is assigned to a trap-assisted recombination mechanism which causes a sublinear photocurrent response with light intensity, slightly overestimating the EQE as we have previously reported in hybrid Bi_2S_3-P3HT systems.[31]

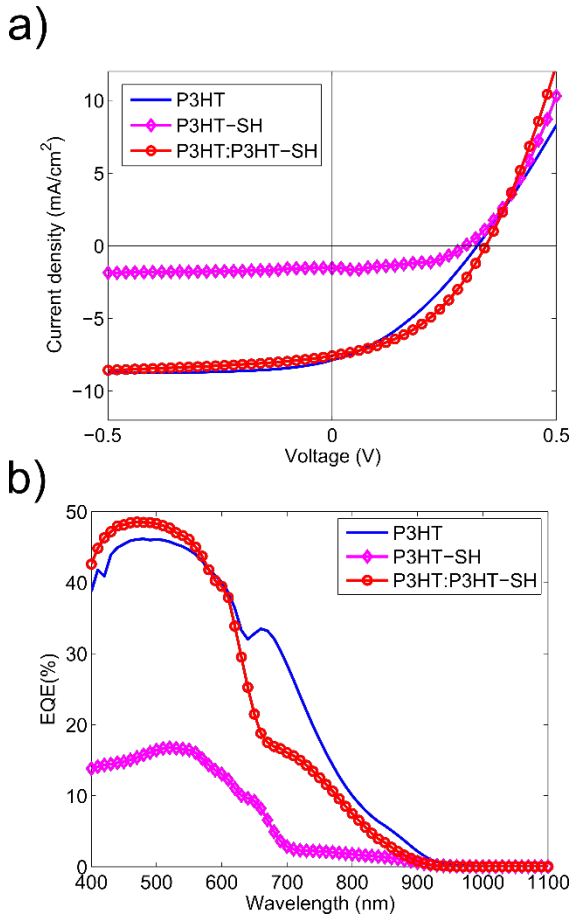

Figure 7 (a) Current voltage characteristics of bulk heterojunctions based on Bi_2S_3 and P3HT solar cells under the irradiation of AM1.5 100 mWcm^{-2} simulated solar light and (b) external quantum efficiency plots based on Bi_2S_3 and P3HT (blue line), Bi_2S_3 and P3HT-SH (magenta line with diamonds) and Bi_2S_3 and a 70:30 wt. mixture of P3HT and P3HT-SH (red line with circles).

E Experimental Section

E1 Materials for the synthesis of thiol-functionalized block copolymer

2-Bromo-3-hexyl-5-iodothiophene was used as received. 2-Bromo-3-hexyl-5-iodo(6-bromohexyl)thiophene was prepared following the previous reports.[21]

E2 Synthesis of Bi_2S_3 nanocrystals

Bismuth sulfide nanocrystals were synthesized using a previously reported method.[31] Briefly, 5.4 mmol of Bi(OAc)3, 34 mmol of oleic acid (OA) and 34 mmol of 1-Octadecene (ODE) were pumped under vacuum overnight at 100ºC. After this time, the reaction temperature was raised to 170ºC. When the reactions flask reaches this temperature, 1.2 mmol of HMS (Hexamethyldisilathiane) mixed with 10 ml of ODE were quickly injected to the flask and the heating temperature was lowered to 100ºC. After 2 h at 100ºC the reaction was quenched by removing the heating mantle and adding 20 ml of cold toluene and 40 ml of cold methanol. The oleate-capped Bi_2S_3 nanocrystals were isolated after centrifugation. Purification of the nanocrystals was performed by successive dispersion/precipitation in toluene/MeOH. Finally the nanocrystals were dispersed in chloroform. Transmission Electron Microscopy pictures, size distribution and XRD studies are available in Supplementary Information.

Individual chloroform solutions of Bi_2S_3, P3HT and P3HT-SH were prepared at a concentration of 50 g/L. The products were mixed at the desired wt. ratio and left stirring overnight inside a nitrogen-filled glovebox. A separate P3HT solution in 1,2-dichlorobenzene was prepared at a concentration of 40 g/L to be employed as the hole-transporting layer.

E3 Material characterization

Gel permeation chromatography (GPC) was performed on a Shimadzu Prominence system equipped with a UV detector and columns (TSK-gel G3000HXL and TSK-gel G5000XL) using CHCl3 as the eluent at 40°C. The sample solutions were filtered by PTFE filter (pore size: 0.2 µm) before the injection. ^{1}H NMR (500 MHz) spectra were measured on a JEOL Alpha FT-NMR spectrometer equipped with an Oxford superconducting magnet system. UV−VIS spectra were recorded on a JASCO V-650 spectrophotometer.

Solution photoluminescence quenching measurements were performed in a Hitachi F-4500 fluorescence spectrometer using a 550 nm excitation. For PL measurements, pristine P3HT or P3HT-SH was mixed with Bi_2S_3 in a chloroform solution at 70:30 wt. ratio.

Solid-state photoluminescence quenching measurements were performed in a Horiba Jovin-Yvon fluorolog system using an integrating sphere. The samples were illuminated with a 450 nm monochromatic light source. The emission of the samples was normalized to their absorbance at 450 nm, measured using a Cary 5000 UV-VIS-NIR spectrophotometer.

Transient Absorption Spectroscopy (TAS) measurements were performed by exciting the sample films, under a dynamic nitrogen atmosphere, with the output from an optical parametric oscillator (Oppolette) pumped by the Nd:YAG laser. The pulse widths of the excitations were 20 ns. The excitation wavelengths used were either 700 nm to excite exclusively the Bi_2S_3 nanocrystals or 510 nm to excite both the Bi¬2S3 and the polymer with a frequency of 20 Hz. The laser intensities used were ~10 or 13.7 µJcm−2, respectively to keep the approximate number of excitation photons the same for all measurements. All readings were normalized to the sample's absorption at the excitation wavelengths. A 100 W quartz halogen lamp (Bentham, IL 1) with a stabilized power supply (Bentham, 605) was used as a probe light source, with a probe wavelength of 1000 nm used. The probe light passing through the sample film was detected with a silicon photodiode (Hamamatsu Photonics, S1722-01). The signal from the photodiode was amplified before passing through electronic band-pass filters (Costronics Electronics). The amplified signal was collected with a digital oscilloscope (Tektronics, TDS220), which was synchronized with a trigger signal from the pump laser pulse from a photodiode (Thorlabs Inc., DET210). To reduce stray light, scattered light, and sample emission, two monochromators and appropriate optical cut-off filters were placed before and after the sample.

Cyclic-voltammetry measurements were performed in 0.1M tetrabutylammonium perchlorate in acetonitrile solution using a CH instruments electrochemical workstation system. We employed a standard three electrode electrochemical cell configuration under nitrogen purge. 5μL of a 10g/L chloroform solution were placed onto a platinum working electrode and let dry. The scan range was set to -2 to 2V and scan speed was set to 0.1V/s starting towards reduction potentials. Silver/silver nitrate 0.1M in acetonitrile reference and platinum wire counter electrodes were calibrated against ferrocene as an internal reference of the system (0.64V vs SHE). Energy levels with respect to vacuum energy were calculated from the potential of the standard hydrogen electrode (SHE = 4.44eV), as previously reported.[32] The HOMO levels were calculated from the onset of the first oxidation potential peak.

E4 Device fabrication

ITO-coated glass substrates were first washed in acetone for 10 minutes followed by 10 minutes bath in ethanol, both under strong sonication. The substrates were then rinsed with abundant DI water and dried with nitrogen. A ZnO ETL layer was then grown using a sol–gel method. Briefly, 0.5 g of zinc acetate dihydrate was dissolved in 5 mL of methoxyethanol and 0.142 mL of ethanolamine. The solution was spin-cast onto the ITO-coated glass substrates at 3000 rpm and cured at 200ºC for 30 minutes. The bismuth sulfide and polymer blend (P3HT, P3HT-SH or mixture of the two) was then spincasted on top of the ETL at 3000 rpm and subjected to a ligand exchange process in a 10 minutes bath in 1,2-ethanedithiol (EDT) 1% vol in acetonitrile (ACN). The unreacted ligands were removed in an ACN bath followed by annealing on a hotplate at 110ºC for 7 minutes. A second layer of the blend product was then spincasted while spinning the substrate, followed by an additional EDT 1% in ACN bath, rinsing and annealing steps (110ºC for 7 minutes). Next, a drop of P3HT solution in 1,2-dichlorobenzene (DCB) at a concentration of 40 g/L was deposited onto the spinning (3000 rpm) substrate as the HTL, followed by a last annealing step at 110ºC for 7 minutes. Finally, the MoO3 (15 nm) and Ag (150 nm) electrodes were thermally evaporated in a Kurt J. Lesker Nano36 system.

E5 Solar cell characterization

Current–voltage characteristics were obtained using a Keithley 2400 source measuring unit (SMU) under dark and simulated AM1.5 solar conditions (Newport Oriel Sol3A). External quantum efficiency (EQE) measurements were obtained using a Newport Cornerstone 260 monochromator and a Keithley 2400 SMU providing short-circuit conditions.

We have prepared the cross-sections for the scanning electron micrographs by focused ion beam (FIB) milling (Zeiss Auriga 60 FIB-SEM, 1-nm-resolution GEMINI scanning electron microscope (SEM)). To protect the upper metal film during FIB milling, we have deposited a thin layer of Pt by ion-beam induced deposition inside the FIB system. The cross-sections are milled using a current of 50 pA at 30 kV. The scanning electron micrographs are taken at an angle of 36° with respect to the sample surface using an In-lens detector and 5 kV acceleration voltage.

Conclusions

In conclusion, we have introduced the synthesis of a new thiol-functionalized block copolymer as a new route to electronically couple hybrid organic-inorganic nanocomposites, based on metal-chalcogenide nanocrystal electron acceptors, while at the same time controlling their nanomorphology and improving the photovoltaic performance. The strong affinity of thiol moieties with the surface of metal chalcogenide nanocrystals allows for a ~50% exciton quenching efficiency. These results, together with the larger degree of polaron formation observed in solid state when employing this new thiol-functionalized block copolymer, suggests an increased electronic interaction between the NCs and the thiol-functionalized block copolymer. When combined with P3HT, an energy cascade which favours charge separation can be formed, further increasing the polaron formation. After careful optimization of the device processing conditions, 15% higher power conversion efficiencies were obtained as a result of the improved nanomorphology and higher opencircuit voltages arisen from the deeper energy levels. Further improvements can be expected if functional groups can be incorporated in the novel semiconductor polymers, such as PCPDTBT or employing functionalized hetero-block copolymer where each block is only responsible and optimized for the roles of charge dissociation or charge transport.

Acknowledgements

We acknowledge financial support from Fundació Privada Cellex, Barcelona and funding from European Commission's Seventh Framework Programme for Research under contract PIRG06-GA-2009-256355, PIEF-GA-2011-298596, and N4E GA.248855. The research leading to these results has received funding from the European Community's Seventh Framework program (FP7-ENERGY.2012.10.2.1) under grant agreement 308997. Portions of this research were carried out at the Stanford Synchrotron Radiation Lightsource, a national user facility operated by Stanford University on behalf of the US Department of Energy, Office of Basic Energy Sciences. Sean Sweetnam is supported by a Benchmark Stanford Graduate Fellowship. This research was also supported in part by Strategic International Cooperative Program, Japan Science and Technology Agency (JST) and MICINN.

Notes and references

[a] ICFO-Institut de Ciencies Fotoniques, Mediterranean Technology Park, 08860, Castelldefels, Barcelona, Spain,.

[b] Department of Applied Chemistry, School of Engineering, The University of Tokyo, Tokyo 113-8656, Japan.

[c] Centre for Plastic Electronics and Department of Chemistry, Imperial College London, South Kensington Campus, Exhibition Road, SW7 2AZ, U.K.

[d] Department of Materials Science and Engineering, Stanford University, Stanford, CA 94305, USA.

[e] RIKEN Center for Emergent Matter Science (CEMS), 2-1 Hirosawa, Wako, Saitama 351-0198, Japan.

[f] Japan Science and Technology Agency, Precursory Research for Embryonic Science and Technology, 4-1-8 Honcho, Kawaguchi, Saitama 332-0012, Japan.

Electronic Supplementary Information (ESI) available: [1H NMR images of P3HT-SH, transient absorption spectra measurements of P3HT and P3HT-SH, photoelectron spectroscopy and hole mobility studies of P3HT

and P3HT-SH and optimization of the hybrid organic-inorganic solar cells are available in the Electronic Supplementary Information.]. See DOI: 10.1039/b000000x/

1 L. Zhao, Z. Lin. *Advanced Materials*, 2012, **24**, 4353.

2 S.A. McDonald, G. Konstantatos, S. Zhang, P.W. Cyr, E.J.D. Klem, L. Levina, E.H. Sargent *Nature Materials*, 2005, **4**, 138.

3 P. Reiss, E. Couderc, J. De Girolamo, A. Pron. *Nanoscale*, 2011, **3**, 446.

4 S. Dayal, N. Kopidakis, D.C. Olson, D.S. Ginley, G. Rumbles, *Nano Letters*, 2010, **10**, 239.

5 J. Seo, M. Cho, D. Lee, A.N. Cartwright, P.N. Prasad, *Advanced Materials*, 2011, **23**, 3984.

6 S.D. Oosterhout, M.M. Wienk, S.S van Bavel, R. Thiedmann, L.J.A. Koster, J. Gilot, V. Schmidt, R.A.J Janssen, *Nature Materials*, 2009, **8**, 818.

7 L.-I. Hung, C.-K., Tsung, W. Huang, P. Yang. *Advanced Materials*, 2010, **22**, 1910.

8 Y.-Y., Lin, D-Y., Wang, H-C., Yen, H-L., Chen, C-C., Chen, C-M., Chen, C-Y., Tang, C-W, Chen. *Nanotechnology*, 2009, **20**, 405207.

9 L. Martinez, A. Stavrinadis, S. Higuchi, S.L. Diedenhofen, M. Bernechea, K. Tajima, G. Konstantatos. *Physical Chemistry Chemical Physics PCCP*, 2013, **15**, 5482.

10 N. Bansal, F.T.F O'Mahony, T. Lutz, S.A. Haque. *Advanced Energy Materials*, 2013, **3**, 986.

11 H.-C., Liao, M.-C., Wu, M.-H., Jao, C.-M., Chuang, Y.-F., Chen, W.-F., Su. *CrystEngComm*, 2012, **14**, 3645.

12 Y.-Y., Lin, T.-H., Chu, S.-S., Li, C.-H., Chuang, C.-H., Chang, W.-F., Su, C.-P., Chang, M.-W., Chu, C.-W. Chen, *Journal of the American Chemical Society*, 2009, **131**, 3644.

13 G. Yu, J. Gao, J.C. Hummelen, F. Wudl, A.J. Heeger. *Science*, 1995, **270**, 1789.

14 J.-F., Lin, W.-C., Yen, C.-Y., Chang, Y.-F., Chen, W.-F., Su, *Journal of Materials Chemistry A*, 2013, **1**, 665.

15 J. Liu, T. Tanaka, K. Sivula, A.P. Alivisatos, J.M.J. Fréchet. *Journal of the American Chemical Society*, 2004, **126**, 6550.

16 S.D. Oosterhout, L.J.A. Koster, S. van Bavel, J. Loos, O. Stenzel, R. Thiedmann, V. Schmidt, B. Campo, T.J. Cleij, L. Lutzen, D. Vanderzande, M.M. Wienk, R.A.J. Janssen. *Advanced Energy Materials*, 2011, **1**, 90.

17 M.C. Iovu, E.E. Sheina, R.R. Gil, R.D. McCullough. *Macromolecules*, 2005, **38**, 8649.

18 R. Miyakoshi, A. Yokoyama, T. Yokozawa. *Journal of the American Chemical Society*, 2005, **127**, 17542.

19 D.A.R. Barkhouse, A.G. Pattantyus-Abraham, L. Levina, E.H. Sargent. *ACS Nano*, 2008, **2**, 2356.

20 N.C. Greenham, X. Peng, A.P. Alivisatos. *Phys. Rev. B. Condensed Matter*, 1996, **54**, 17628.

21 S. Miyanishi, Y. Zhang, K. Hashimoto, K. Tajima. *Macromolecules*, 2012, **45**, 6424.

22 M.A. Ruderer, S. Guo, R. Meier, H-Y., Chiang, V. Körstgens, J. Wiedersich, J. Perlich, S.V. Roth, P. Müller-Buschbaum. *Advanced Functional Materials*, 2011, **21**, 3382.

23 D. Zhitomirsky, M. Furukawa, J. Tang, P. Stadler, S. Hoogland, O. Voznyy, H. Liu, E.H. Sargent. *Advanced Materials*, 2012, **24**, 6181.

24 W.C. Tsoi, S.J. Spencer, L. Yang, A.M. Ballantyne, P.G. Nicholson, A. Turnbull, A.G. Shard, C.E. Murphy, D.D.C. Bradley, J. Nelson, J.-S. Kim. *Macromolecules*, 2011, **44**, 2944.

25 J. Veres, S. Ogier, G. Lloyd, D. de Leeuw. *Chemistry of Materials*, 2004, **16**, 4543.

26 M.J. Greaney, S. Das, D.H. Webber, S.E. Bradforth, R. Brutchey. L. *ACS Nano*, 2012, **6**, 4222.

27 M. Graetzel, R.A.J. Janssen, D.B. Mitzi, E.H. Sargent. *Nature*, 2012, **488**, 304.

28 T. Ameri, J. Min, N. Li, F. Machui, D. Baran, M. Forster, K.J Schottler, D. Dolfen, U. Scherf, C.J. Brabec. *Advanced Energy Materials*, 2012, **2**, 1198.

29 I.J. Kramer, L. Levina, R. Debnath, D. Zhitomirsky, E.H. Sargent. *Nano Letters*, 2011, **11**, 3701.

30 I.J. Kramer, E.H. Sargent. *ACS Nano*, 2011, **5**, 8506

31 L. Martinez, M. Bernechea, F.P.G de Arquer, G. Konstantatos. *Advanced Energy Materials*, 2011, **1**, 1029.

32 E. Kucur, J. Riegler, G.A. Urban, T.J. Nann. *The Journal of Chemical Physics*, 2003, **119**, 2333.